Int J Adv Manuf Technol (2012) 59:491–505
DOI 10.1007/s00170-011-3513-1

ORIGINAL ARTICLE

Analysis of deep drawing of sheet metal using the Marform process

Maziar Ramezani · Zaidi Mohd Ripin

Received: 1 October 2010 / Accepted: 4 July 2011 / Published online: 22 July 2011

Abstract This paper deals with the deep drawing of metal cups using the Marform process. Using this technique, higher limiting drawing ratios can be obtained compared with the conventional deep drawing process. The analytical model of the process is presented initially, followed by the finite element simulations using ABAQUS software. A new friction model based on local contact conditions is presented and used in the finite element (FE) simulations of the process. Compared with traditional Coulomb friction model, the results of the FE simulations with the new friction model showed good correlation with experimental results. The results showed that the maximum thinning occurs at the punch profile portion, and by increasing the forming pressure, thinning of the sheet metal propagates from the punch profile portion to the side wall. At low forming pressures, wrinkles appear in the flange, whilst at higher pressures, fracture is the main defect of the Marform process.

Keywords Deep drawing · Marform process · Friction model · Rubber die

Nomenclature

Roman symbols

A_n	Nominal contact area (m^2)
A_r	Real contact area (m^2)
F_f	Friction force (N)
F_n	Normal load (N)
F_{stmax}	Maximum static friction force (N)
F_t	Tangential load (N)
g	Elasticity of the springs in SLS model (Pa)
h	Separation (m)
h	Punch stroke (m)
K_1	Ratio of the forming pressure in the blank holder portion to the average forming pressure
K_2	Ratio of the forming pressure in the side wall of the blank to the average forming pressure
n	Density of asperities (m^{-2})
P	Pressure (Pa)
r_0	Instant outside radius of deformed blank (m)
r_1	Distance from axis of punch to boundary of forming radius portion and flange (m)
r_p	Punch profile radius (m)
R_0	Initial radius of blank (m)
R_2	Radius of punch (m)
t	Thickness of blank (m)
y_0	Distance from neutral surface of blank at flange to boundary of forming radius portion and side wall (m)
z	Surface height (m)

Greek symbols

β	Mean radius of asperity (m)
ε	Strain
ν	Poisson's ratio
η_d	Viscosity of dashpot in SLS model (Pa s)
δ_n	Normal approach (m)
δ_t	Tangential displacement (m)
$\varphi_{(t)}$	Creep compliance function (Pa^{-1})
$\psi_{(t)}$	Stress relaxation function (Pa)
ρ_d	Forming radius of neutral surface at angle of φ (m)
φ_1	Angle of contact between deformed blank and punch (deg)
μ	Coefficient of friction
μ_c	Coulomb coefficient of friction
$\theta(\overline{s})$	Normalized Gaussian height distribution
σ_s	Standard deviation of the asperity heights (m)

M. Ramezani (✉) · Z. M. Ripin
School of Mechanical Engineering, Universiti Sains Malaysia, 14300 Nibong Tebal, Penang, Malaysia
e-mail: mzramezani@gmail.com

σ_φ Meridian stress (Pa)
σ_θ Circumferential stress (Pa)
σ_{r1} Radial stress at boundary between forming radius portion and flange (Pa)
σ_e Average yield stress of blank material (Pa)

1 Introduction

Marform process is a technique for deep drawing of sheet metals with a rubber die. It was developed by the Glen L. Martin Company in the USA [1] to apply the inexpensive tooling of the Guerin process to the deep drawing operation. It is most suitable for the drawing of cups with high drawing ratios and the forming of wrinkle-free shrink flanges. As shown in Fig. 1, this process uses a thick rubber pad and a form block similar to the Guerin process [2], with the additional independent blank holder plate and a hydraulic cylinder with a pressure-regulating valve.

The rubber pad in this process is kept inside a container attached to the press ram. The thickness of the rubber pad is normally 1.5–2 times as thick as the total depth of the cup, including trim allowance. A throw sheet is usually used between the rubber and the blank to protect the rubber pad from scratching or scoring. The throw sheet could be either cemented to the rubber pad or just laid over the blank. The punch is fixed to the press table. The pressure-regulating valve controls the pressure applied to the blank through the blank holder during the process.

The process starts with the blank being clamped between the rubber pad and blank holder plate above the punch. As the press ram moves down, the rubber pad starts to deform and, together with an appropriate blank holder pressure, pushes the blank to the punch and forces it to draw and take the shape of the punch. During the process, the pressure-regulating valve releases fluid at a controlled rate to provide proper blank holder force. The blank holder pressure must be high enough to avoid wrinkling of the flange. On the other hand, a too high blank holder pressure increases the necessary ram force, which may cause tearing in the blank. Therefore, the blank holder pressure should be regulated properly between these two opposite effects.

There are very few research on the Marform process available in the literature. Fukuda and Yamaguchi [3] carried out an experimental and theoretical analysis of the process. They reported that a drawing ratio of 2.76 could be achieved using the Marform process. In another work, Fukuda et al. [4] carried out first-stage drawing and redrawing experiments using the Marform process and studied the effect of forming pressure, blank thickness and pressure path on the process. They introduced a so-called S character-type pressure path which makes the drawing operation more successful. Venkatesh and Goh [5] introduced a simplified mathematical model for cup drawing using the Marform process. They used a factorial experimental design to obtain the mathematical model and found that the blank thickness is the major factor affecting the limiting drawing ratio of the Marform process. Browne and Battikha [6] carried out an experimental study of the rubber pad forming process to investigate the capabilities of the process and optimize the process parameters. The effect of the key process parameters on the Guerin and Marform processes was discussed in this paper to produce a defect-free

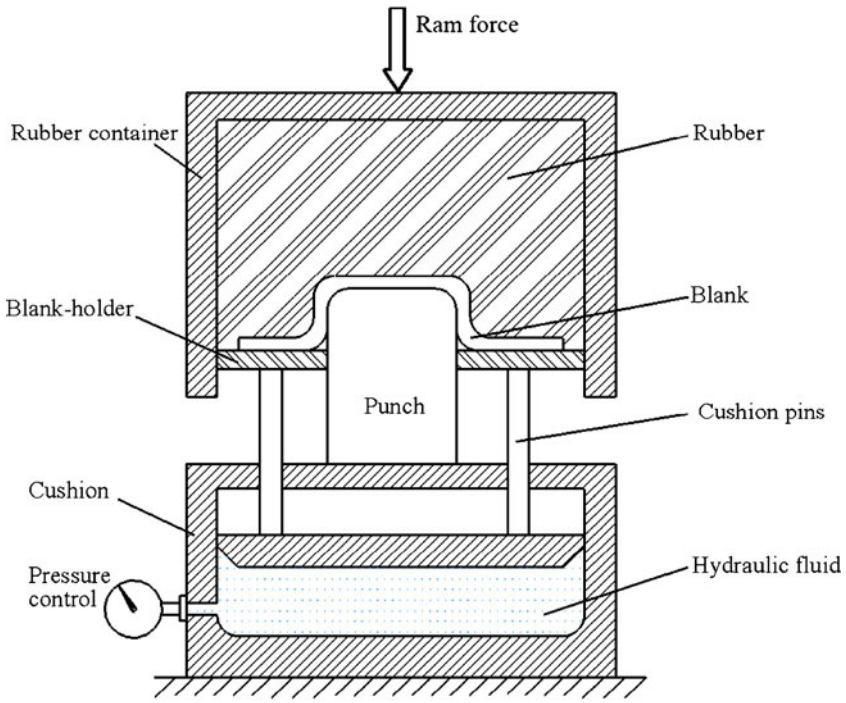

Fig. 1 Schematic drawing of the Marform process

product. Thiruvarudchelvan [7] developed a software on sheet metal and tube forming processes using flexible pressure-carrying media which illustrates the advantages and disadvantages of different forming processes including the Marform technique.

In the present work, an analytical analysis has been carried out followed by finite element (FE) simulations to investigate the effect of the key process parameters on deep drawing of sheet metals using the Marform technique. To the best of the authors' knowledge, this is the first time that an FE analysis of the Marform process is presented. Moreover, a new friction model for rubber/metal contact is presented in this paper, which allows the determination of coefficient of friction as a function of local contact conditions such as roughness, rubber characteristics and contact pressure. Such a comprehensive friction model is used in the FE simulation of the Marform process rather than the often used Coulomb friction model. The relationship between the thickness distribution, punch stroke, forming pressure and forming limit diagram during the drawing operation is presented in this paper. Comparison between the results obtained by the FE simulations and the experimental results are carried out.

2 Theoretical analysis of the Marform process

The analytical model presented in this section is based on the work of Fukuda and Yamaguchi [3]. They considered a volume element at the forming radius portion of the blank, as shown in Fig. 2. The equilibrium equations of the force components acting on this volume element are shown in the figure. The dimensional reference diagram of the cup is shown in Fig. 3. Assuming that the friction coefficient is constant and the blank thickness does not change during the

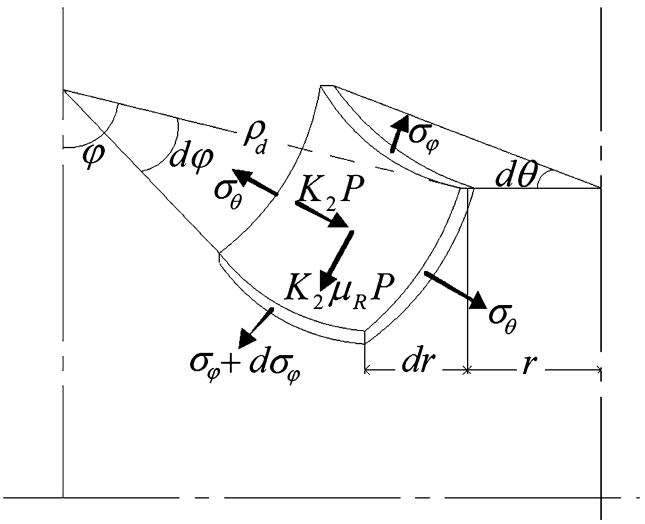

Fig. 2 Volume element at the forming radius portion

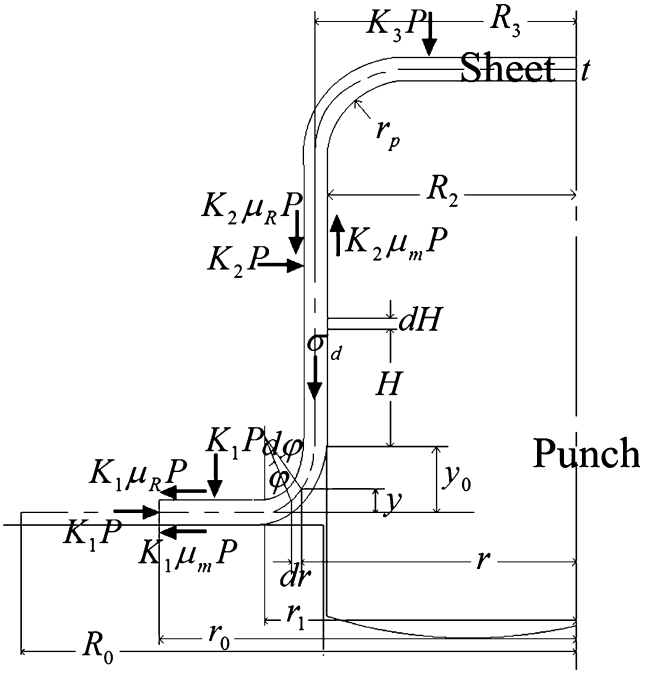

Fig. 3 Dimensional reference diagram of the cup

process and considering the blank material as a perfectly plastic solid, they could derive the following equation:

$$\frac{\mathrm{d}(\sigma_\varphi/\sigma_e^*)}{\mathrm{d}\varphi} = \left(\frac{\sigma_\varphi}{\sigma_e^*}\right) \frac{\cos\varphi + \mu_R K_2 (P/\sigma_e^*)(r/R_2)/(t/R_2)}{(\sigma_\varphi/\sigma_e^* - 1)\sin\varphi + K_2(P/\sigma_e^*)(r/R_2)/(t/R_2)} \tag{1}$$

where σ_e is the average yield stress of the blank material; σ_φ and σ_θ are the meridian and circumferential stresses, respectively; t is the thickness of the blank; P is the average forming pressure; K_2 is the ratio of forming pressure in the side wall of the blank to the average forming pressure; ρ_d is the forming radius of neutral surface at angle of φ; μ_R is the coefficient of friction between rubber and sheet metal; R_2 is the radius of punch; and $\sigma_e^* = \frac{2\sigma_e}{\sqrt{3}}$. Considering the geometrical relationship together with Eq. 1, the following relations can also be obtained:

$$\frac{\mathrm{d}(r/R_2)}{\mathrm{d}\varphi} = -\frac{(\sigma_\varphi/\sigma_e^*)(r/R_2)\cos\varphi}{(\sigma_\varphi/\sigma_e^* - 1)\sin\varphi + K_2(P/\sigma_e^*)(r/R_2)/(t/R_2)} \tag{2}$$

$$\frac{\mathrm{d}(y/R_2)}{\mathrm{d}\varphi} = \frac{(\sigma_\varphi/\sigma_e^*)(r/R_2)\sin\varphi}{(\sigma_\varphi/\sigma_e^* - 1)\sin\varphi + K_2(P/\sigma_e^*)(r/R_2)/(t/R_2)} \tag{3}$$

Solving Eqs. 1, 2 and 3 using numerical methods, one can obtain the profile and the stress at the forming radius

portion of blank. To solve these equations numerically, the following initial values can be used:

$$\varphi = 0\,, \quad \sigma_\varphi/\sigma_e^* = \sigma_{r1}/\sigma_e^*\,, \quad r/R_2 = r_1/R_2\,, \quad y/R_2 = 0$$
$$\frac{d(\sigma_\varphi/\sigma_e^*)}{d\varphi} = \left(\frac{\sigma_{r1}}{\sigma_e^*}\right)\frac{1+\mu_R K_2(P/\sigma_e^*)(r_1/R_2)/(t/R_2)}{K_2(P/\sigma_e^*)(r_1/R_2)/(t/R_2)}$$
$$\frac{d(r/R_2)}{d\varphi} = -\frac{(\sigma_{r1}/\sigma_e^*)}{K_2(P/\sigma_e^*)/(t/R_2)}, \frac{d(y/R_2)}{d\varphi} = 0 \tag{4}$$

The term σ_{r1}/σ_e^* in Eq. 4 can be expressed as:

$$\frac{\sigma_{r1}}{\sigma_e^*} = \ln\frac{(r_0/R_2)}{(r_1/R_2)} + \frac{K_1(\mu_R+\mu_m)(P/\sigma_e^*)((r_0-r_1)/R_2)}{(t/R_2)} - K_1(P/\sigma_e^*) \tag{5}$$

where μ_m is the coefficient of friction between the blank and the blank holder and K_1 is the ratio of forming pressure in the blank holder portion to the average forming pressure. The term $K_1(P/\sigma_e^*)$ on the right-hand side of Eq. 5 indicates the influence of the pressure acting radially on the periphery of the blank.

Assuming that the total area of blank is unchanged during drawing, the following correlations can be achieved for the angle of contact between the deformed blank and the punch φ_1 (see Fig. 4), the punch stroke h and the instant radius of blank r_0. For the case of $\varphi_1 \le 90°$, they can be expressed as follows:

$$h/R_2 = y_0/R_2 + (\rho_p/R_2)(1-\cos\varphi_1) \tag{6}$$

$$\left(\frac{r_0}{R_2}\right)^2 = \left(\frac{R_0}{R_2}\right)^2 + \left(\frac{r_1}{R_2}\right)^2 - \left(\frac{R_3-\rho_p}{R_2}\right)^2 - 2\int_0^{\varphi_1}\frac{r}{R_2}\frac{\rho_d}{R_2}d\varphi - 2\left(\frac{\rho_p}{R_2}\right)\left[\left(\frac{R_3-\rho_p}{R_2}\right)\varphi_1 + \left(\frac{\rho_p}{R_2}\right)(1-\cos\varphi_1)\right] \tag{7}$$

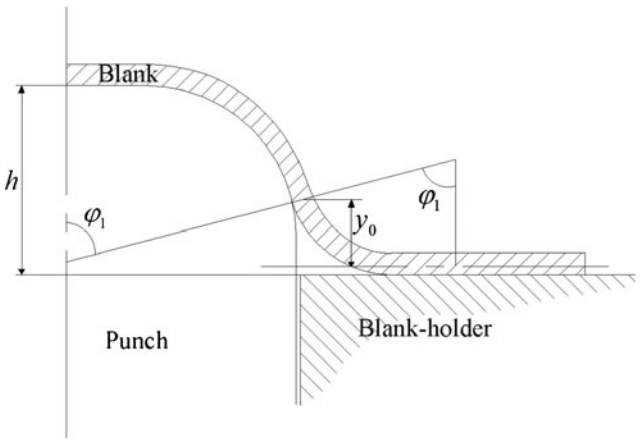

Fig. 4 Forming radius portion profile

After the side wall is formed, Eq. 7 becomes:

$$\left(\frac{r_0}{R_2}\right)^2 = \left(\frac{R_0}{R_2}\right)^2 + \left(\frac{r_1}{R_2}\right)^2 - \left(\frac{R_3-\rho_p}{R_2}\right)^2 - 2\int_0^{\pi/2}\frac{r}{R_2}\frac{\rho_d}{R_2}d\varphi - 2\left(\frac{\rho_p}{R_2}\right)\left[\left(\frac{R_3-\rho_p}{R_2}\right)\frac{\pi}{2} + \left(\frac{\rho_p}{R_2}\right)\right] - \frac{2}{R_2}(h-y_0-\rho_p) \tag{8}$$

where $\rho_p = r_p + t/2$ and r_p is the punch profile radius. $R_3 = R_2 + t/2$ and r_1 is the distance from the axis of punch to the boundary of forming radius portion and flange, as shown in Fig. 3. R_0 is the initial radius of blank and y_0 is the distance from the neutral surface of blank at flange to the boundary of forming radius portion and side wall.

Equations 1, 2 and 3 can be solved simultaneously using numerical techniques such as Runge–Kutta method to obtain values for $\sigma_\varphi/\sigma_e^*$, r/R_2, y/R_2 and ρ_d/R_2. The initial values given by Eq. 4 can be determined by selecting, in an arbitrary manner, the values of r_0/R_2 and r_1/R_2.

On the other hand, we have the following geometrical relationship in the practical drawing process:

$$r_{\varphi_1} = R_2 - r_p + \rho_p \sin\varphi_1 \tag{9}$$

Therefore, the numerical calculations should be repeated until the value of $r_{\varphi 1}$ obtained by solving the differential equations agrees with the value calculated from Eq. 9. By changing the value of r_1/R_2 at small intervals during the numerical calculations, the reliable value of r_1/R_2 corresponding to a fixed value of r_0/R_2 can be achieved, and so the coordinate $(r/R_2, y/R_2)$ can be determined.

3 Analysis of friction between rubber and blank

In a metal forming process, the conditions in all different contacts are very different. For most forming simulations, the value of coefficient of friction is assumed to be constant, neglecting the fact that friction depends on a large number of parameters, e.g. the micro-geometry, the macro-geometry, the lubricant and the operational parameters: velocity, temperature and normal load [8]. Often, several metal forming simulations with different values of the friction coefficient have to be carried out before the simulation gives acceptable results. It is clear that these kinds of simulations have no predicting power and that a friction model based on local contact conditions is needed [9].

Due to the high contact pressure between the blank and the rubber ring in the Marform process, the friction has a great effect on the forming force and forming limit of the blank. Therefore, it is very important to know the coefficient of friction at the contact surface between the

blank and the rubber pad as a function of contact pressure. In this section, a multi-asperity friction model between viscoelastic asperities and a rigid flat under combined normal and tangential loading conditions is developed for rubber/metal contact, taking into account the viscoelastic behaviour of rubber and local contact conditions.

3.1 Coulomb friction model

The easiest and probably the most well-known friction model is the Coulomb friction model. This friction model is widely used to describe the friction in mechanical contacts, although it greatly oversimplifies the frictional phenomena. In this model, the ratio between the friction force and the normal force, defined as the coefficient of friction, is considered to be constant. The Coulomb friction model can be formulated as:

$$F_{\mathrm{f}} = \mu_c F_{\mathrm{n}} \tag{10}$$

where μ_{c} is the Coulomb coefficient of friction, F_{f} is the friction force and F_{n} the normal load in the contact.

3.2 Multi-asperity friction model for rubber/metal contact

When two solids are pushed together, they do not make atomic contact everywhere within the apparent contact area, and contact happens only on peak asperities of surfaces [10]. To model the contact between rough surfaces, it is required to find out the contact parameters between the pair of asperities carrying the load. For two elastic spherical asperities loaded by a normal force, F_{n}, Hertz's [11] theory is the basic theory for specifying the radius of the contact circle, the pressure and the normal approach. For the case when a tangential force, F_{t}, is subsequently applied, the tangential displacement of asperities and the shear stress within the contact can be achieved by Mindlin's [12] theory. He described the contact region as a stick area in the centre of contact between a pair of asperities bordered by an annulus area of micro-slip across the edge of the contact. Johnson [13] presented a solution for this micro-slip region.

Rubber materials show both elasticity and viscous resistance to deformation. These materials can hold the elastic strain energy partially and at the same time dissipate energy by continuing the deformation [9]. Rubber materials can be modelled using springs and dashpots connected in series and/or in parallel. A dashpot connected in parallel with a spring, shown in Fig. 5a, is called a Voigt element. If deformed, the force in the spring is supposed to be proportional to the elongation of the assembly, and the force in the dashpot is supposed to be proportional to the rate of elongation of the assembly. If a sudden tensile force is applied to the Voigt model, some of the work done in the assembly is dissipated in the dashpot and the rest is stored in the spring.

A dashpot connected in series with a spring is called Maxwell element and is shown in Fig. 5b. In this model, if a sudden tensile force is applied, the total displacement of the element is the sum of the displacements of the spring and the dashpot. In fact, the response of rubber to stress or strain change is a combination of both mentioned models (see Fig. 5c). The response is always time-dependent and involves both the elastic storage of energy and viscous loss.

The standard linear solid (SLS) model provides a good explanation of both stress relaxation and creep behaviour. Stress relaxation is the time-dependent decrease in stress under constant strain at constant temperature. For the SLS model, the generalized Hook's equation is:

$$\eta_d g_1 \ \dot{\varepsilon} + g_1 g_2 \varepsilon = \eta_{\mathrm{d}} \ \dot{\sigma} + (g_1 + g_2) \cdot \sigma \tag{11}$$

where g_1,g_2 are the elasticity of springs, η_{d} is the viscosity of the dashpot, ε is the strain and σ is the stress.

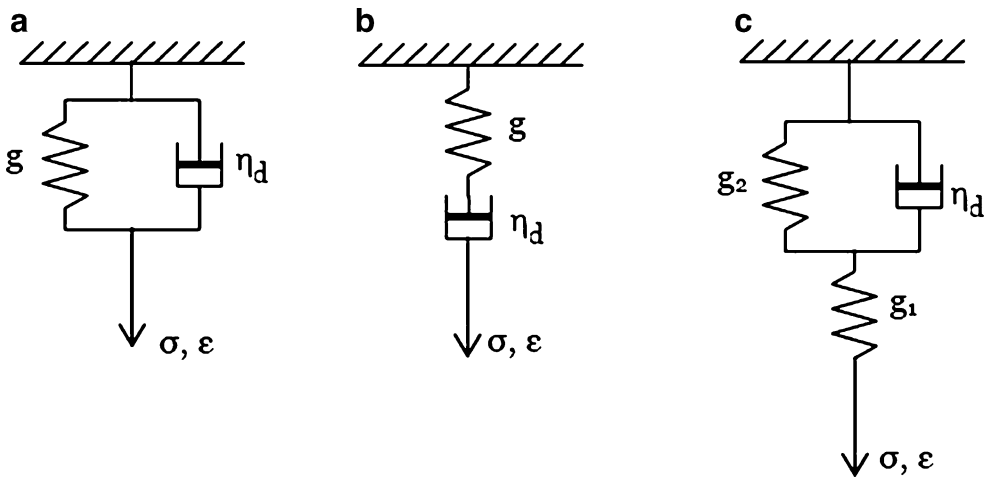

Fig. 5 Mechanical models representing the response of viscoelastic materials: **a** Voigt model, **b** Maxwell model, **c** SLS model

At constant stress equal to σ_0, and by solving Eq. 11 with respect to the strain ε, we reach the creep compliance function $\varphi(t)$ as:

$$\varphi(t) = \frac{\varepsilon(t)}{\sigma_0} = \frac{1}{g_1} + \frac{1}{g_2}\,[1 - \exp(\frac{-t}{T_2})] \tag{12}$$

where $T_2 = \frac{\eta_d}{g_2}$ is the retardation time.

In the same way, the stress relaxation function $\psi(t)$ can be achieved by considering the strain constant and is equal to ε_0 in Eq. 11:

$$\psi(t) = \frac{\sigma(t)}{\varepsilon_0} = \frac{g_1}{g_1 + g_2}\,[g_2 + g_1\,\exp(\frac{-t}{T_2})] \tag{13}$$

where $T_2 = \frac{\eta_d}{(g_1+g_2)}$ is the retardation time.

Surface roughness can be modelled as a set of spherical asperities with the same radius where their heights follow a Gaussian distribution (see Fig. 6). Three parameters for the description of random rough surfaces are the average asperity radius, β (spherical-shaped asperities); the asperity density, n; and the standard deviation of the asperity heights, σ_s. Based on the experiments of Greenwood and Williamson [14], most surfaces have a value in the range of 0.03–0.05 for the product $n\beta\sigma_s$.

Hui et al. [15] presented a model for viscoelastic/rigid contacts under several loading conditions such as constant load test, load relaxation test and constant displacement rate test. In their theory, analytical solutions are presented for the real contact area and the total normal load. The case of a viscoelastic rough surface which is normally loaded against a rigid surface is considered in this paper.

3.2.1 Normal loading of viscoelastic/rigid multi-asperity contact

For a certain separation h, the number of asperities in contact at a certain separation can be determined by:

$$n_c = A_n\, n \int_{\overline{h}}^{\infty} \theta(\overline{s})\mathrm{d}\overline{s} \tag{14}$$

where A_n denotes the nominal contact area, $\overline{s} = \frac{s}{\sigma_s}$ is the normalized asperity height, $\overline{h} = \frac{h}{\sigma_s}$ is the normalized separation, and $\theta(s)$ is the normalized Gaussian height distribution which can be obtained as:

$$\theta(\overline{s}) = \frac{1}{\sqrt{2\pi}}\; e^{-\frac{\overline{s}^2}{2}} \tag{15}$$

Then, the real contact area can be calculated by:

$$A_r = A_n\, n\, \beta\, \sigma_s\, \pi \int_{\overline{h}}^{\infty} (\overline{s} - \overline{h})\, \theta(\overline{s})\mathrm{d}s \tag{16}$$

The total normal load can also be obtained as the sum of all normal loads carried by the asperities in contact.

$$F_n = A_n\, n\, \beta^{\frac{1}{2}}\, \sigma_s^{\frac{3}{2}}\, \frac{8}{3}\, \frac{1}{\phi(t)} \int_{\overline{h}}^{\infty} (\overline{s} - \overline{h})^{\frac{3}{2}}\, \theta(\overline{s})\mathrm{d}\overline{s} \tag{17}$$

3.2.2 Tangential loading of viscoelastic/rigid multi-asperity contact

In this section, we consider that the multi-asperity contact presented in Section 3.2.1 is subsequently loaded by an increasing tangential load. At a certain separation and for a tangential load smaller than the force required starting macro-sliding (maximum static friction force), the multi-contact interface is composed of micro-contacts in the partially slip regime and micro-contacts totally sliding. Macro-sliding occurs if all contacting asperities are in the fully sliding regime [12].

Bureau et al. [16] described a condition for an elastic multi-contact interface which gives a critical asperity height above which the micro-contacts are partially sliding. In their work, a constant local friction coefficient is used for all micro-contacts. Using Bureau's method, the critical asperity height for a viscoelastic multi-contact interface is:

$$\delta_{tv}(t) = \delta_n(t)\,\mu\,(2-\nu)\,[1 - (1 - \frac{F_t}{\mu \cdot F_n})^{\frac{2}{3}}] \tag{18}$$

where δ_{tv} is the preliminary displacement and μ is the local coefficient of static friction. Rearranging the factors in Eq. 18, we will have:

$$1 - \frac{\delta_{tv}(t)}{\delta_n(t)\,\mu\,(2-\nu)} = (1 - \frac{F_t}{\mu \cdot F_n})^{\frac{2}{3}} \tag{19}$$

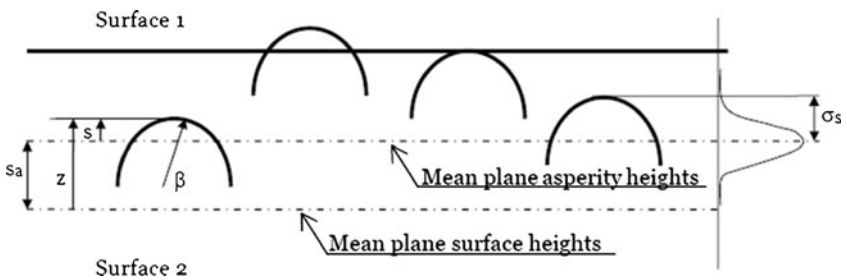

Fig. 6 Contact model of rough surfaces

The right-hand side of Eq. 19 is a positive real number for $F_t \leq \mu \cdot F_n$; so,

$$\frac{\delta_{tv}(t)}{\mu\,(2-\nu)} \leq \delta_n(t) \tag{20}$$

The indentation depth of the asperity δ_n can be replaced by $(z - h)$. Then, the inequality 20 becomes

$$z \geq \frac{\delta_{tv}(t)}{\mu\,(2-\nu)} + h \tag{21}$$

Therefore, from Eq. 21, the asperities having the height

$$s_c \leq \frac{\delta_{tv}(t)}{\mu\,(2-\nu)} + h \tag{22}$$

are in the fully sliding regime as they carry a tangential force which is equal to or larger than the maximum static friction force. The micro-contacts of which heights satisfy the relation $z \geq s_c$ are in the partially slip regime.

The total tangential load carried by the multi-contact interface is:

$$F_t = F_{stick} + F_{slip} \tag{23}$$

where F_{stick} is the sum of all tangential loads carried by the micro-contacts which are not fully sliding. Deladi [17] obtained the following equation for F_{stick} component:

$$F_{stick}(t) = A_n\, n\, \sigma_s^{\frac{3}{2}}\, \frac{8}{3}\, \frac{1}{\varphi(t)}\, \beta^{\frac{1}{2}} \int_{\overline{s}_c}^{\infty} (\overline{s} - \overline{h})^{\frac{3}{2}}\, \theta(\overline{s})\, \mu \left[1 - \left(1 - \frac{\delta_t}{(2-\nu)\,(\overline{s} - \overline{h})\,\mu\,\sigma_s}\right)^{\frac{3}{2}}\right] d\overline{s} \tag{24}$$

The F_{slip} component is taken as the sum of all tangential loads carried by the fully sliding micro-contacts:

$$F_{slip}(t) = A_n\, n\, \sigma_s^{\frac{3}{2}}\, \frac{8}{3}\, \frac{1}{\phi(t)}\, \beta^{\frac{1}{2}} \int_{\overline{h}}^{\overline{s}_c} (\overline{s} - \overline{h})^{\frac{3}{2}}\, \theta(\overline{s})\, \mu\, d\overline{s} \tag{25}$$

Obtaining the tangential load carried by the multi-contact interface, the maximum static friction force can be calculated as the sum of all tangential loads causing gross sliding of all micro-contacts [17]. When this condition is obeyed, the partially sliding component F_{stick} becomes zero and the condition becomes:

$$F_{stmax} = F_{slip} \qquad if \quad F_{stick} = 0 \tag{26}$$

Therefore, the static coefficient of friction is:

$$\mu_s = \frac{F_{stmax}}{F_n} \tag{27}$$

The algorithm for calculating the maximum static friction force and coefficient of static friction is depicted in Fig. 7. Determining the micro-geometry, the nominal area of contact and the material properties, the real area of contact, A_r, and the normalized separation, $\overline{h}$, can be calculated using Eqs. 16 and 17. Then, by assuming a tangential displacement, the critical height, s_c, can be obtained from Eq. 22. Next, the tangential loads carried by each micro-contact can be calculated from Eqs. 24 and 25. If the partially stick component of the tangential force is not zero, the tangential displacement should be increased until all micro-contacts are fully sliding. This maximum tangential displacement corresponding to the occurrence of macro-sliding is the global limiting displacement. Finally, the maximum static friction force is obtained and the static coefficient of friction can be determined from Eq. 27.

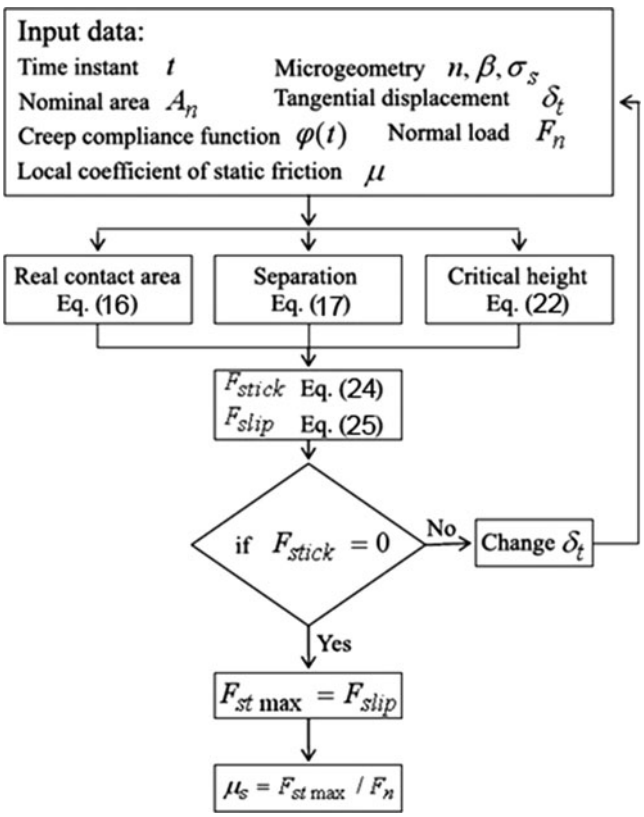

Fig. 7 Algorithm for the calculation of coefficient of friction

4 Finite element simulations

Many FE simulations are available in the literature for conventional and hydrodynamic deep drawing processes (see, e.g. [18–20]); however, there are no published simulation results for deep drawing using the Marform process. ABAQUS/Standard finite element code is used in this paper to simulate the Marform process and predict material deformation during forming. Due to the axisymmetric character of the forming, only a 2D model was used to reduce computation time. The punch and blank holder were assumed to be rigid, and the blank was modelled as a deformable material using CAX4R (a four-node bilinear axisymmetric quadrilateral, reduced integration, hourglass control) elements. The flexible rubber was modelled using CAX4RH elements. The dimensions of blank and tools used in the FE simulation are illustrated in Table 1. Penalty contact interfaces were used to enforce the contact and the sliding boundary condition between the blank and the tools. The coefficient of Coulomb friction is fixed at 0.15 for contact surfaces between blank and metallic tools. This value is based on the results of friction analysis of rubber pad forming process conducted previously by the authors (see [8]). The coefficient of friction between rubber and blank changes with contact pressure based on the model presented in Section 3. The contact pressure-dependent coefficients of friction are implemented to the model through the contact property option of ABAQUS programme. This option is used to introduce friction properties into the mechanical surface interaction models.

The simulation begins with the punch in contact with the blank. The flexible rubber then moves down to draw the blank. The interfaces between the tools and the blank are modelled using an automatic surface-to-surface contact algorithm. The blank material is an ASTM-A36 structural steel. The material properties for the blank were determined from a tensile test performed on the blank material according to the ASTM E 8M standard. The constitutive behaviour of blank is described by an elastic–plastic model. For the elastic part, Young's modulus of 210 GPa and Poisson's ratio of 0.3 is used. For the plastic part, the hardening model is assumed to be isotropic described by the power law approach:

$$\sigma = K\,\varepsilon^{n} \tag{28}$$

where σ is the flow stress (MPa), ε is the total true strain (dimensionless), K is the strength coefficient (MPa) and n is the strain-hardening exponent (dimensionless). The material properties of the ASTM-A36 structural steel are listed in Table 2.

Natural rubber with Shore A hardness of 60, elastic modulus of 59.65 MPa, Poisson's ratio of 0.49997 and density of 1,200 kg/m^3 is used as the flexible tool. A compression test was carried out according to the ASTM D575 standard to determine the material properties of natural rubber. Both tensile and compression tests were carried out using model 3367 INSTRON universal testing machine. The stress–strain diagram of natural rubber under compression is shown in Fig. 8. Rubber is made of an isotropic, nonlinear, hyper-elastic, incompressible, strain history-independent material. Hyper-elastic materials are described in terms of a strain energy potential, W, which defines the strain energy stored in the material per unit of reference volume (volume in the initial configuration) as a function of the strain at that point in the material [9]. Among several forms of strain energy potentials available in ABAQUS, Ogden (N=3) strain energy is used for rubber modelling. Ogden's [21] material model has previously been used with success to predict the behaviour of hyper-elastic materials (see, e.g. [22]). The form of Ogden strain energy potential is:

$$\sigma_{ij} = \frac{\partial W}{\partial \varepsilon_{ij}} \tag{29}$$

$$W = \sum_{i=1}^{N} \frac{2\mu_i}{\alpha_i^2}\left(\overline{\lambda}_1^{\alpha_i} + \overline{\lambda}_2^{\alpha_i} + \overline{\lambda}_3^{\alpha_i} - 3\right) + \sum_{i=1}^{N} \frac{1}{D_i}\left(J^{el} - 1\right)^{2i} \tag{30}$$

where W is the strain energy per unit of reference volume; $\overline{\lambda}_i$ is the deviatoric principal stretch which can be defined

Table 1 Dimensions of the tools for FE simulations

Parameters	Values
Punch radius, R_2 (mm)	14
Punch nose radius, r_p (mm)	5
Blank initial radius, R_0 (mm)	35
Blank initial thickness, t_0 (mm)	1
Rubber height (mm)	45
Rubber radius (mm)	38

Table 2 Property specification of the ASTM-A36 structural steel

Parameters	Values
Yielding stress, σ_{yield} (MPa)	245
Ultimate tensile stress, σ_{ult} (MPa)	400
Young's modulus, E (GPa)	210
Poisson's ratio, v	0.3
Density, ρ (kg/m^3)	7,800
Strain-hardening exponent, n	0.23
Hardening coefficient, K (MPa)	545

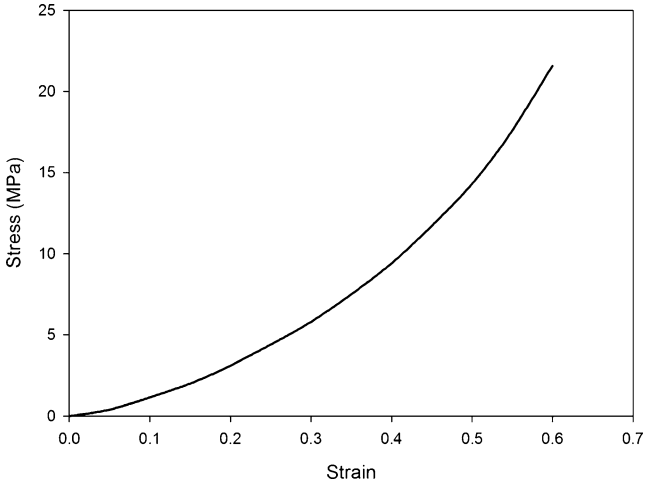

Fig. 8 Stress–strain diagram of natural rubber under compression

by $\overline{\lambda}_i = J^{-\frac{1}{3}}\lambda_i$; λ_i is the principal stretch; J^{el} is the elastic volume ratio; and μ_i, α_i and D_i are temperature-dependent Ogden constants. Compressibility can be defined by specifying nonzero values for D_i, by setting the Poisson's ratio to a value <0.5, or by providing test data that characterize the compressibility. We assumed a fully incompressible behaviour for rubber with v=0.4997 and D_i equal to zero, and so the second expression in Eq. 30 can be eliminated. To determine the strain energy density, W, ABAQUS uses a least-squares fitting algorithm to evaluate the Ogden constants automatically from experimental data.

5 Results and discussion

5.1 Coefficient of friction and FE simulations

The Alicona imaging infinite focus microscope (IFM 2.1) was employed to determine the surface parameters of natural rubber. Surface parameters in terms of density of asperity n, mean radius of asperity β and standard deviation of the asperity heights σ_s are the input parameters of the friction model explained in Section 3. Figure 9 illustrates the roughness profile along a selected line in the surface of natural rubber. The geometrical parameters stated above can be attained by these measurements using the Alicona microscope.

The viscoelastic material parameters in terms of spring elasticity, g_1,g_2, and dashpot viscosity, η_d, of the SLS model are other input parameters of the friction model. The values of viscoelastic material parameters used in the calculations of the friction model are achieved from the stress relaxation test of rubber. In a stress relaxation test, a compressive strain at a constant rate within a very brief period of time is applied on an unconstrained cylinder and the stress required maintaining the compressive strain is recorded in time. The test is performed according to the ASTM D 6048 standard. Stress relaxation modulus as a function of time (see Eq. 13) for natural rubber of Shore hardness A 60 is demonstrated in Fig. 10. According to Eqs. 12 and 13, for $t\rightarrow 0$, we obtain $\psi(0)=\varphi(0)^{-1}=g_1$, and for $t\rightarrow\infty$, we have $\varphi(\infty)=\psi(\infty)^{-1}=\frac{g_1+g_2}{g_1\cdot g_2}$. The values of input parameters for the calculation of the coefficient of friction as a function of contact pressure are listed in Table 3.

Using the values of parameters in Table 3 as input values for the friction model presented in Section 3, the coefficient of friction between rubber and blank as a function of contact pressure is calculated (see Fig. 11). It can be seen from Fig. 11 that an increase in contact pressure decreases the coefficient of friction. At low pressures, this decrease is more important than at higher loads when the coefficient of friction reaches a fairly stable level. This is in agreement with the observation of Benabdallah [23] where experimental work on some thermoplastics against steel and aluminium showed a similar effect.

The distribution of von Mises stresses at the last stage of the simulation is shown in Fig. 12. The maximum FE-predicted von Mises stress for blank at the last step of the forming process is 472.5 MPa. The distribution of von Mises stress in natural rubber at the end of the process is shown in Fig. 13. As illustrated in the figure, the maximum

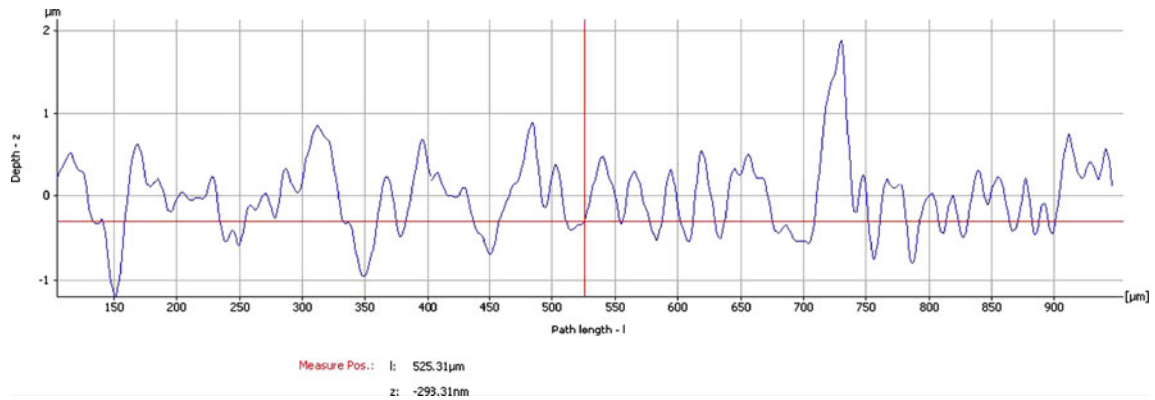

Fig. 9 Roughness profile of natural rubber

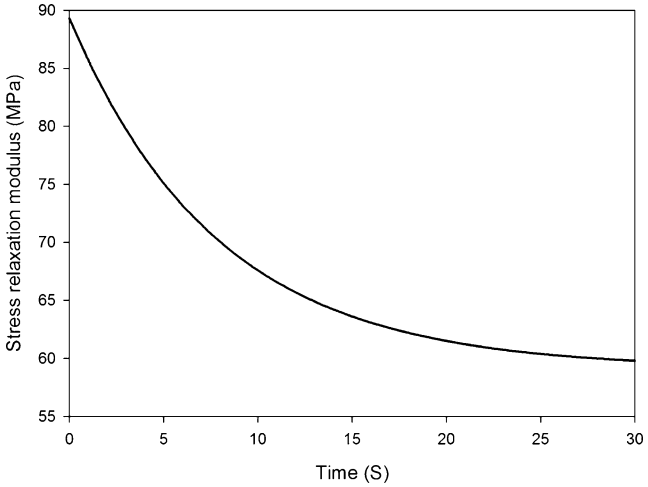

Fig. 10 Stress relaxation modulus as a function of time for natural rubber

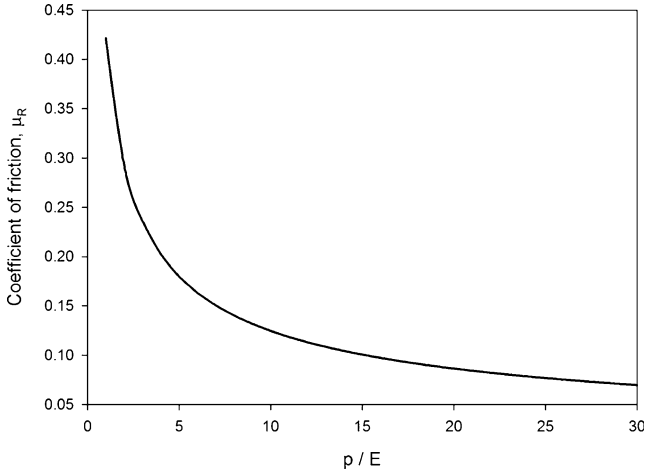

Fig. 11 Coefficient of friction between natural rubber and steel as a function of forming pressure

von Mises stress in the rubber is 18 MPa and occurs at the punch nose region.

5.2 Pressure distribution at different potions of rubber pad

In the FE simulations, forming pressure was kept constant during the process and was applied to the top of the rubber die. A parametric study was carried out by changing the values of rubber container diameter, D, and punch diameter, d_p. Forming pressure distributions in different regions of the rubber die were measured using FE simulations.

Figure 14 shows the pressure distribution at different portions of the rubber die as a function of D/d_p. In this figure, K represents the ratio of forming pressure at different portions of the rubber die to the forming pressure which is applied to the top of the rubber die during FE simulation. As illustrated in the figure, the pressure at the portions of the punch top and the blank holder are almost same. On the other hand, the pressure distribution at the side wall portion and forming radius portion are relatively the same, but are always lower than the value at the punch top and blank holder portions. The pressure at each portion reaches a quite constant value after $\frac{D}{d_p} \geq 3$.

Table 3 Values of the input parameters for friction model

Parameters	Values
n (m^{-2})	2.9×10^{11}
β (μm)	0.525
σ_s (μm)	0.305
g_1 (Pa)	8.93×10^{7}
g_2 (Pa)	1.75×10^{-8}
η_d (Pa s)	2.08×10^{9}
μ	0.4

5.3 Results of analytical approach

Based on the analytical approach presented in Section 2, numerical calculations were carried out using the dimensions of the FE model listed in Table 1. The forming pressure distributions were expressed by the approximate values of $K_1=K_3=1$ and $K_2=0.8$, which were obtained from FE simulations as presented in Fig. 14.

Figure 15 shows the effect of forming pressure, P, on variation of r_1 at different angles of contact between the deformed blank and the punch (see Fig. 4). As depicted in the figure, the value of r_1 decreases with increasing the

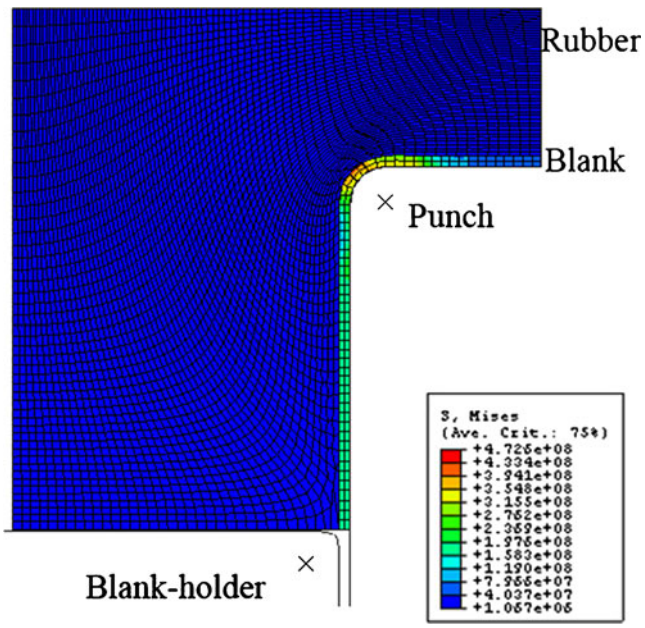

Fig. 12 Distribution of von Mises stress at the last stage of the process

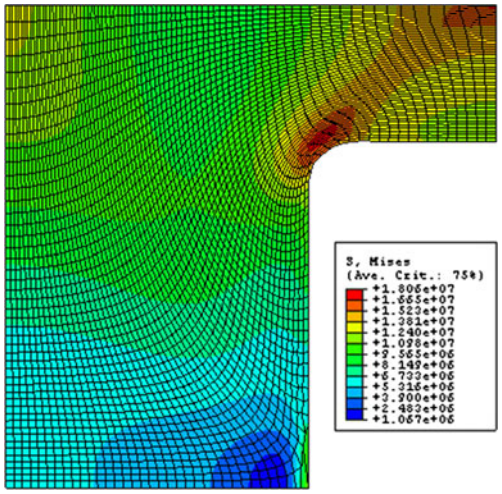

Fig. 13 Distribution of von Mises stress in natural rubber

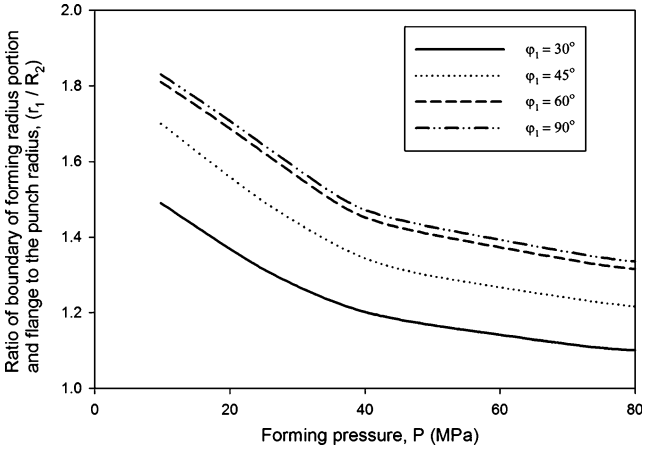

Fig. 15 Influence of forming pressure on the deformation of the forming radius portion

forming pressure. It shows that at lower pressures, the bending radius between the cup wall and flange increases. According to this figure, drawing of the cups with smaller bend radius needs higher forming pressure.

Figure 16 shows the influence of forming pressure on the outside radius of blank, r_0. As illustrated in the figure, before the side wall is formed completely, i.e. $\varphi_1<90°$, forming pressure does not have a great effect on r_0. However, as the side wall is formed, i.e. $\varphi_1=90°$, the influence of forming pressure becomes remarkable, and an increase in forming pressure results in an increase in r_0.

Figures 17 and 18 show the variations of r_1 and y_0 vs. r_0 after the side wall is formed ($\varphi_1=90°$) at different forming pressures. Both values increase as r_0 increases. An increase in the value of forming pressure results in the decrease of r_1 and y_0. In other words, the larger the value of forming pressure, the smaller the forming radius becomes.

Figure 19a illustrates the variation of the radius of forming boundary, r_1, vs. instant outside radius, r_0, during the Marform process with the forming pressure of 80 MPa. According to Fig. 19a, in the beginning of the stroke, the ratio of r_0/R_2 is large and r_1/R_2 is almost unity, i.e. the workpiece is still flat. As the punch stroke increases, the ratio of r_0/R_2 and r_1/R_2 decreases uniformly, indicating that the blank is now pushed into the rubber die by the punch until it reaches the state of $r_0/R_2=2.2$, where r_1/R_2 reaches its maximum of 1.33. The variation of y_0 vs. r_0 during the process with forming pressure of 80 MPa is shown in Fig. 19b. According to the figure, y_0 increases rapidly and reaches its maximum value at the early stage of forming and after that decreases constantly. In comparison, Fig. 19b also shows that at $r_0/R_2=2.2$, the height of the forming boundary achieves its maximum. As the punch stroke gets bigger, the value of r_1 and y_0 decreases until the process is over and the overall dimensions of $r1$ and y_0 are achieved.

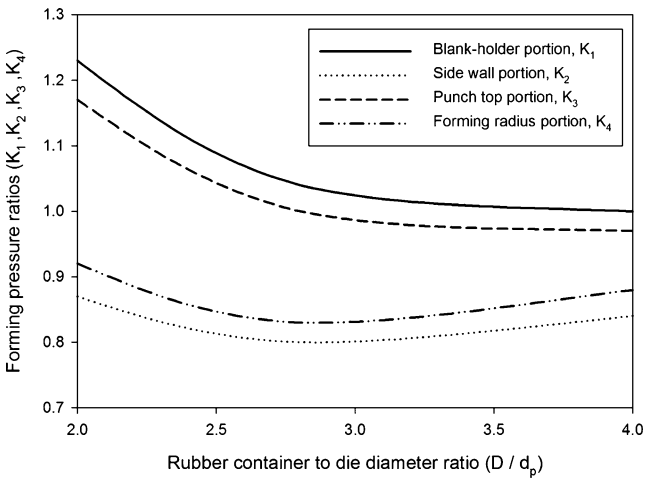

Fig. 14 Forming pressure at different portions of the rubber die

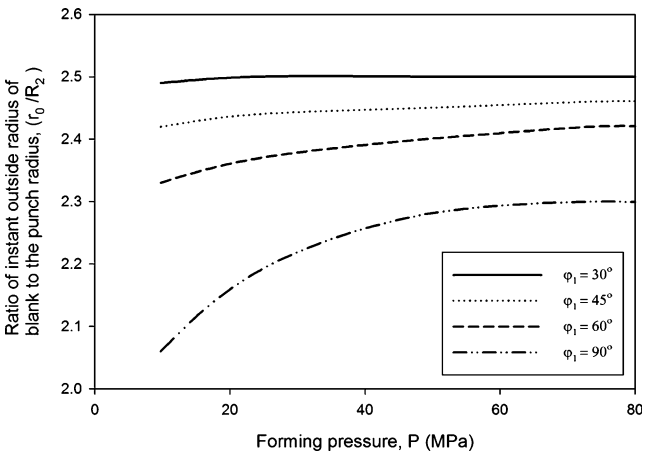

Fig. 16 Influence of forming pressure on the outside radius of blank

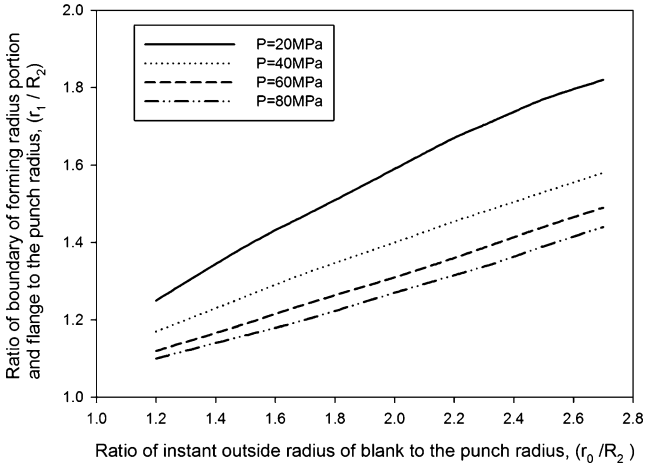

Fig. 17 Variation of r_1 vs. r_0 after the side wall is formed at different forming pressures

The profile at the forming radius portion obtained from analytical analysis is also presented in Fig. 19c. The results are for the case of $\frac{r_0}{R_2} = 2.15$ and forming pressure of 80 MPa.

5.4 Development of thickness strain

The effect of forming pressure and drawing ratio on the thickness strain distribution of the drawn cup was investigated using FE simulations. For fracture analysis, the maximum tensile strain must not exceed the limit strain at which localized necking occurs. Three different values of forming pressure, i.e. 20, 50 and 70 MPa, were used in this study. Figure 20 shows the effect of these forming pressures on the thickness of the drawn cup. As can be seen in the figures, the maximum thinning occurs at the punch profile portion, where the blank is stretched excessively. It can also

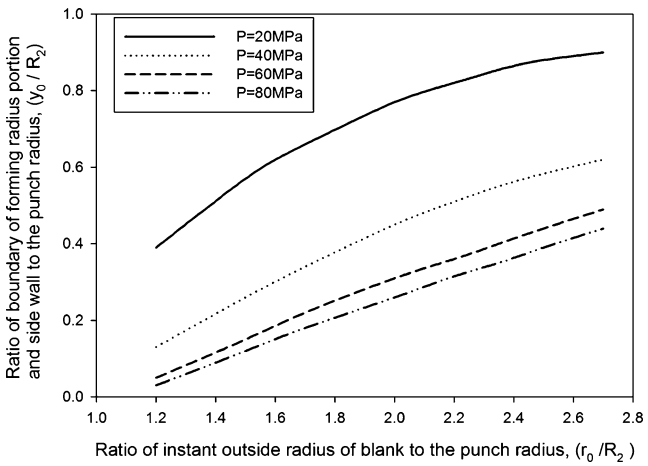

Fig. 18 Variation of y_0 vs. r_0 after the side wall is formed at different forming pressures

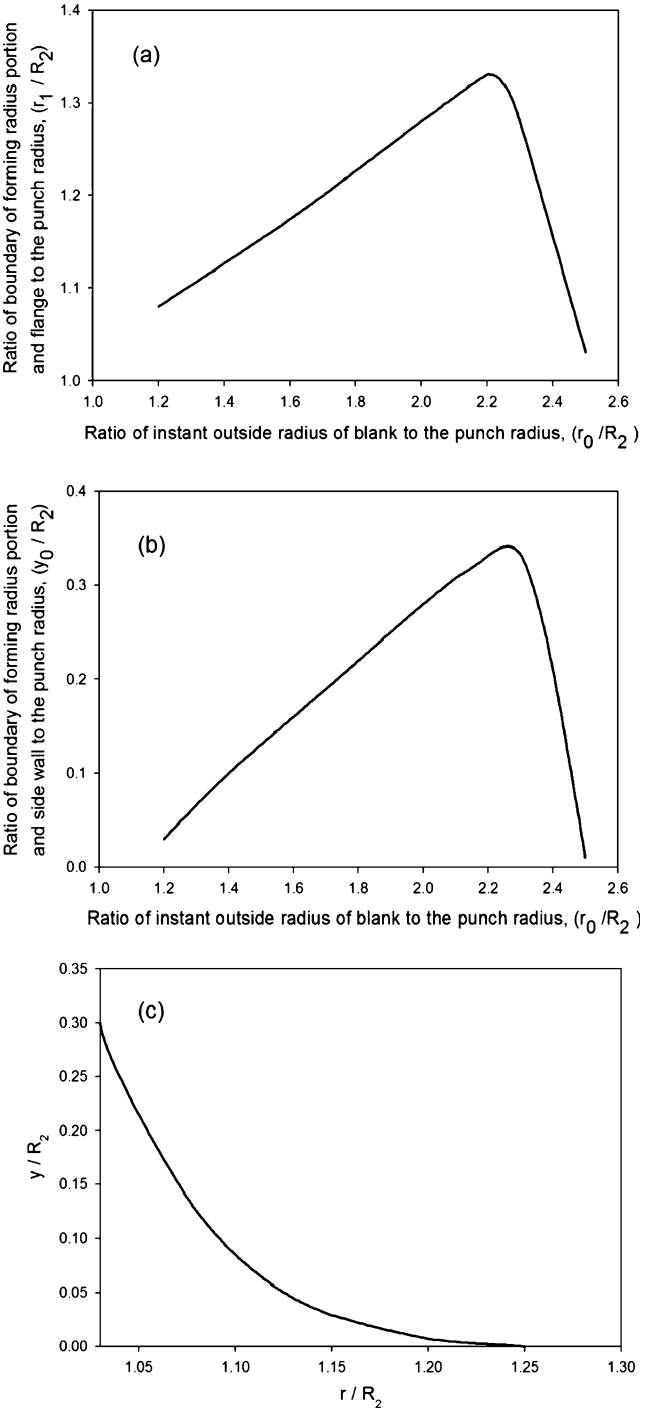

Fig. 19 **a** Variation of the radius of the forming boundary r_1 with the instant outside radius r_0. **b** Variation of y_0 with the instant outside radius r_0. **c** Variation of y vs. r during the forming process

be noted that as the punch stroke increases, the thinning of the cup increases. The results show that using low forming pressure such as 20 MPa, very deep drawn cups cannot be reached as the workpiece fractures at 19-mm stroke and for increasing the value of drawing ratio the forming pressure

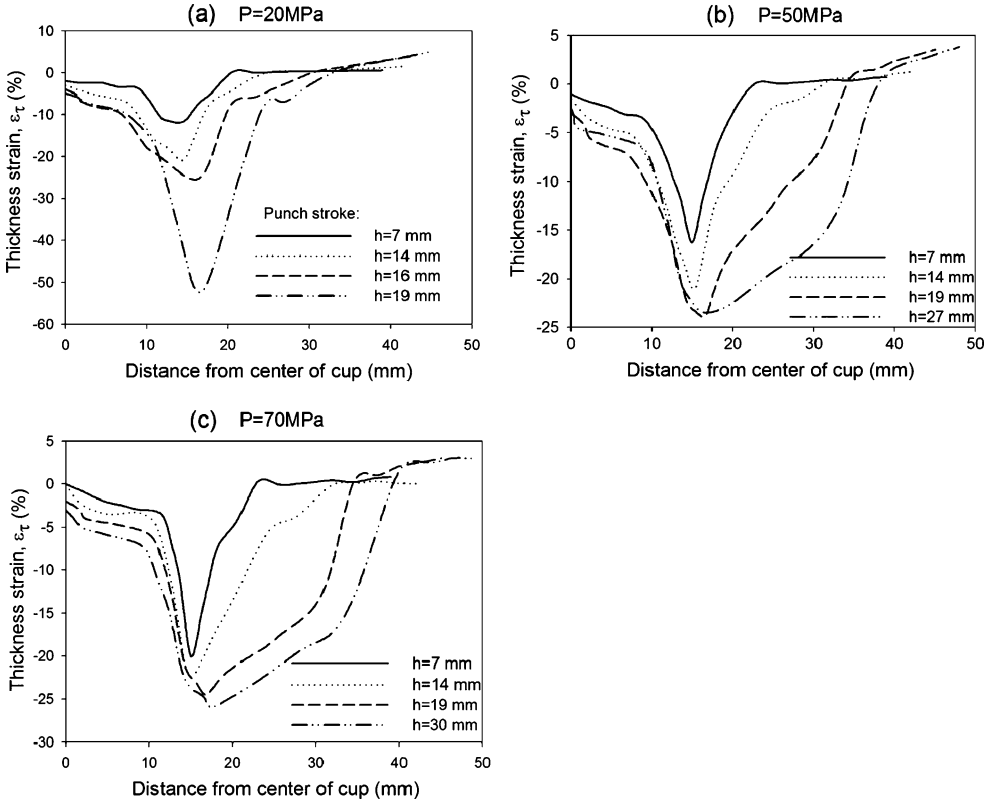

Fig. 20 Development of thickness strain at different forming pressures for various punch strokes

should increase. On the other hand, a very high forming pressure needs higher press capacity. Therefore, for achieving a defect-free drawn cup, these two effects should be considered simultaneously and an optimized forming pressure should be used. It can also be concluded from the results that at low forming pressures, thinning is concentrated at the punch profile portion. As the forming pressure increases, thinning propagates from the punch profile portion to the side wall. This is one of the remarkable characteristics of the Marform technique which helps draw cups with larger drawing ratio compared with the conventional deep drawing process.

The effect of forming pressure on maximum thinning of the blank at the punch profile portion is illustrated in Fig. 21 for different punch strokes. As can be seen in the figure, at low pressures, i.e. $P \leq 40$ MPa, the thickness decreases rapidly at higher strokes, which leads to fracture. At higher forming pressures, i.e. $P \leq 50$ MPa, the thickness decreases uniformly throughout the operation and makes it possible to achieve higher drawing ratios.

To validate the FE simulation of the process with experimental results, a model is built for drawing of SPCE sheet according to the geometry and properties reported in [4]. The development of thickness strain in the drawn cup with two forming pressures of 19.6 and 68.65 MPa and different punch strokes are shown in Figs. 22, 23 and 24. According to the figures, the FE simulations tend to predict more thinning compared with the experimental results. The results of the simulations show that using the new friction model instead of the very often applied Coulomb's friction model has a significant effect on better prediction of thickness distribution. The FE simulations showed that the Coulomb friction model with $\mu=0.3$ has the best match with the experimental results. The maximum thinning at the punch profile portion decreases from $\mu=0$ to $\mu=0.3$ and after that increases due to excessive contact pressure and

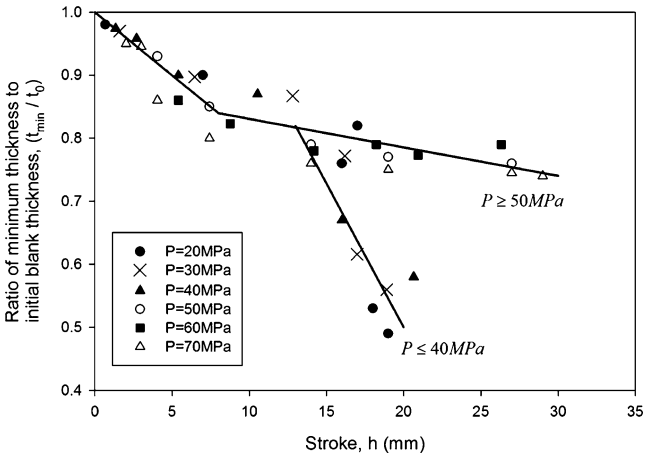

Fig. 21 Variation of minimum thickness at punch profile portion vs. punch stroke

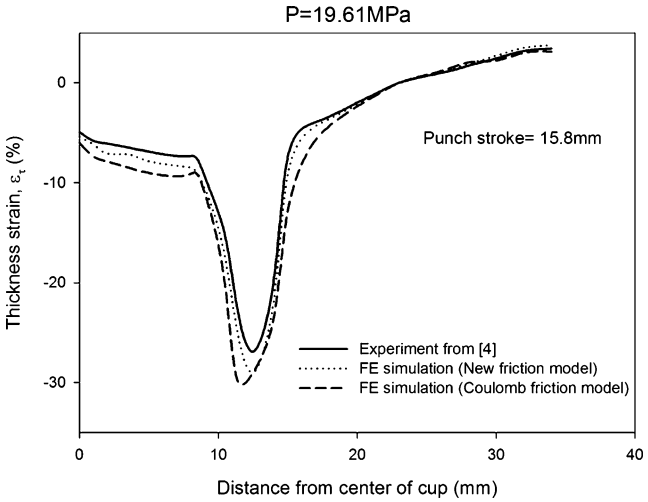

Fig. 22 Comparison of the experimental and FE results for the development of thickness strain at P=19.6 MPa and punch stroke of 15.8 mm

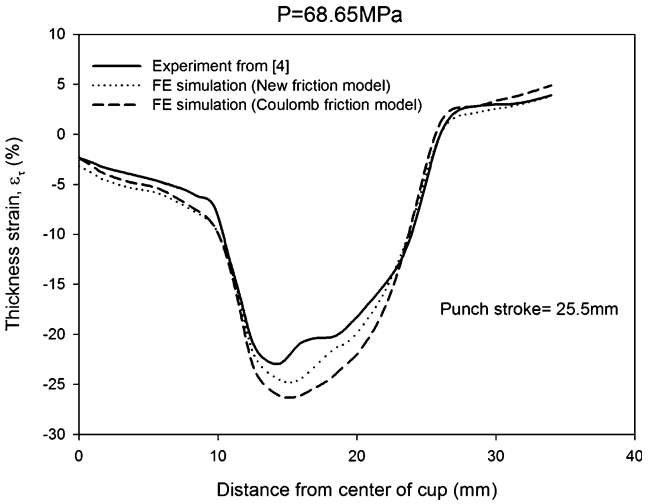

Fig. 24 Comparison of Experimental and FE results for the development of thickness strain at P=68.65 MPa and punch stroke of 25.5 mm

frictional forces. According to Fig. 24, the FE prediction error for thinning at the bend point of the drawn cup is <7% using a new friction model, whilst the error increases to 12.5% using the Coulomb friction model with μ=0.3. It can be seen that Figs. 22 and 23 also show the same trend, and the results of FE simulations with the new friction model and experimental works show a similar tendency and correlate very well with each other in a series of conditions.

5.5 Forming limit diagram

The criteria for wrinkling and fracture of the workpiece are based on the work of Wang et al. [24]. According to their paper, the maximum compressive strain at the flange must not exceed the limit strain at which wrinkling occurs. Based on their analysis, the critical strain to onset wrinkles and fracture depends on both geometric dimensions (thickness and curvatures of sheet) and material properties (Young's modulus, strength coefficient and strain-hardening exponent). The mathematical formulations of the criteria are available at [24]. Based on these equations, the forming limit diagram of the ASTM-A36 structural steel was obtained using FE simulations.

Forming limit diagram is determined by the appearance of fracture and wrinkle of the cup at different forming pressures. Figure 25 shows the forming limit diagram of the ASTM-A36 structural steel in the case of constant forming pressure during the Marform process. The drawn curves separate the safe region from the unsafe region. Using this figure, the relative proximity of wrinkle or fracture of the blank can be determined and forming conditions can be selected accordingly.

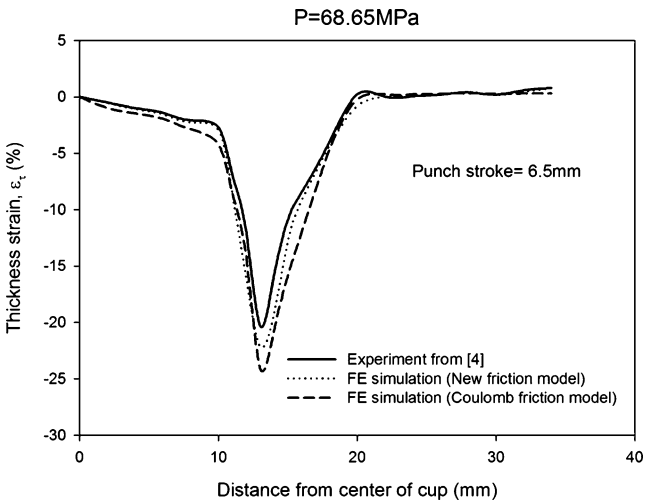

Fig. 23 Comparison of Experimental and FE results for the development of thickness strain at P=68.65 MPa and punch stroke of 6.5 mm

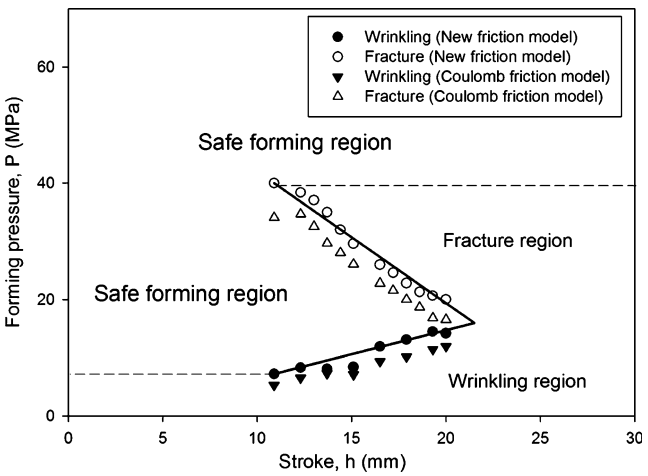

Fig. 25 Forming limit diagram

As can be seen in the figure, wrinkles appear for relatively low pressures. At higher pressures up to 40 MPa, fracture is the main defect of the process. As the forming pressure exceeds 40 MPa, higher drawing ratios can be achieved without fracture by increasing the stroke up to 30 mm. The difference between the forming limit diagram prediction using the new friction model and the Coulomb friction model is also illustrated in the figure. According to the results of FE simulations, the new friction model predicts a larger wrinkling region and a smaller fracture region compared with the results of the Coulomb friction model with μ=0.3.

6 Conclusions

In this paper, the deep drawing of sheet metals using the Marform technique was investigated using analytical model and finite element simulations. The main conclusions of this research are as follows:

- An increase in contact pressure results in a decrease in coefficient of friction between the rubber and the metal. The coefficient of friction reaches a quite constant value at higher normal pressures.
- Using the new friction model instead of the very often applied Coulomb friction model has a significant effect on the accuracy of FE simulations.
- At low forming pressures, thinning is concentrated at the punch profile portion. As the forming pressure increases, thinning propagates from the punch profile portion to the side wall.
- Wrinkles appear in the cup at relatively low pressures. At higher forming pressures, fracture is the main defect of the process.
- Drawing of the cups with smaller bend radius needs higher forming pressure.
- r_1 and y_0 increase rapidly and reach their maximum values at the early stage of forming and after that decrease constantly during the Marform process.

References

1. Thiruvarudchelvan S (1993) Elastomers in metal forming: a review. J Mater Process Tech 39(1–2):55–82
2. Ramezani M, Ripin ZM, Ahmad R (2009) Numerical simulation of sheet stamping process using flexible punch. Proc IMechE, B: J Eng Manuf 223(7):829–840
3. Fukuda M, Yamaguchi K (1971) An analysis for deep drawing of cylindrical shell with rubber die. Bull JSME 14(71):504–511
4. Fukuda M, Yamaguchi K, Muramatsu H (1974) Forming pressure control in first stage drawing and re-drawing of cylindrical shells with rubber die. Bull JSME 17(105):409–420
5. Venkatesh VC, Goh TN (1986) A note on mathematical models of cup drawing by the Guerin and Marform processes. J Mech Work Tech 13(3):273–278
6. Browne DJ, Battikha E (1995) Optimisation of aluminium sheet forming using a flexible die. J Mater Process Tech 55(3–4):218–223
7. Thiruvarudchelvan S (1995) A software on sheet metal forming processes (A) with the aid of flexible tools, (B) using hydraulic pressure. J Mater Process Tech 48(1–4):699–705
8. Ramezani M, Ripin ZM, Ahmad R (2009) Computer aided modelling of friction in rubber-pad forming process. J Mater Process Tech 209(10):4925–4934
9. Ramezani M, Ripin ZM, Ahmad R (2009) A static friction model for tube bulge forming using a solid bulging medium. Int J Adv Manuf Technol 43(3–4):238–247
10. Ramezani M, Ripin ZM (2010) A friction model for dry contacts during metal-forming processes. Int Adv Manuf Technol 51(1–4):93–102
11. Hertz H (1882) Über die Berührung fester elastischer Körper. J Reine Angew Math 92:156–171
12. Mindlin RD (1949) Compliance of elastic bodies in contact. ASME J Appl Mech 16:259–268
13. Johnson KL (1985) Contact mechanics. Cambridge University Press, Cambridge
14. Greenwood JA, Williamson JBP (1966) Contact of nominally flat surfaces. Proc R Soc Lond A 295:300–319
15. Hui CY, Lin YY, Baney JM (2000) The mechanics of tack: viscoelastic contact on a rough surface. J Polym Sci B: Polymer Physics 38:1485–1495
16. Bureau L, Caroli C, Baumberger T (2003) Elasticity and onset of frictional dissipation at a non-sliding multi-contact interface. Proc R Soc Lond A 459(2039):2787–2805
17. Deladi EL (2006) Static friction in rubber–metal contacts with application to rubber pad forming processes. PhD thesis, University of Twente, the Netherlands
18. Singh SK, Dixit A, Kumar DR (2008) Optimization of the design parameters of modified die in hydro mechanical deep drawing using LS-DYNA. Int J Adv Manuf Technol 38(1–2):32–37
19. Saxena RK, Dixit PM (2009) Finite element simulation of earing defect in deep drawing. Int J Adv Manuf Technol 45(3–4):219–233
20. Morovvati MR, Fatemi A, Sadighi M (2011) Experimental and finite element investigation on wrinkling of circular single layer and two-layer sheet metals in deep drawing process. Int J Adv Manuf Technol 54:113–121. doi:10.1007/s00170-010-2931-9
21. Ogden RW (1972) Large deformation isotropic elasticity—on the correlation of theory and experiment for incompressible rubberlike solids. Proc Roy Soc Lond A 326:565–84
22. Ramezani M, Ripin ZM (2010) Combined experimental and numerical analysis of bulge test at high strain rates using split Hopkinson pressure bar apparatus. J Mater Process Tech 210 (8):1061–1069
23. Benabdallah HS (2007) Static friction coefficient of some plastics against steel and aluminum under different contact conditions. Tribol Int 40:64–73
24. Wang CT, Kinzel G, Altan T (1995) Failure and wrinkling criteria and mathematical modeling of shrink and stretch flanging operations in sheet-metal forming. J Mater Process Tech 53:759–780